Journal of Alloys and Compounds 509 (2011) 3042–3047

Contents lists available at ScienceDirect

Journal of Alloys and Compounds

journal homepage: www.elsevier.com/locate/jallcom

Electronic and optical properties of iron pyrite

L. Vadkhiya, B.L. Ahuja*

Department of Physics, University College of Science, M.L. Sukhadia University, Udaipur-313 001, Rajasthan, India

ARTICLE INFO

Article history:
Received 28 July 2010
Received in revised form
30 November 2010
Accepted 30 November 2010
Available online 8 December 2010

PACS:
13.60.Fz
71.15.Ap
72.80.Ga
78.20.Ch

Keywords:
Compton scattering
Basis-set (LCAO
APW)
Transition metal compound
Dielectric function

ABSTRACT

We have computed for the first time the energy bands, density of states and Compton profiles of FeS_2 using linear combination of atomic orbital approach. To interpret the theoretical Compton profiles, we have measured the first ever experimental Compton profiles along [1 1 0] and [1 0 0] directions using 100 mCi ^{241}Am Compton spectrometer. The absolute profiles and the anisotropies in momentum densities are well explained by the hybridisation of Hartree–Fock scheme and density functional theory. In addition, to explore the utility of FeS_2 in photovoltaics, we have also discussed the optical properties using full potential linearised augmented plane wave method.

1. Introduction

Since last three decades, there is a considerable interest in the layered transition-metal dichalcogenides (MX_2: M = transition-metal from IV B, VB, VI B or VIII group, X = S, Se or Te) due to their electrical, optical and magnetic properties [1]. In photo electrochemical cells [2,3], they can be used as electrode materials. These dichalcogenides exhibit band gap well matched with the solar spectrum, hence can be treated as prototype materials for photovoltaic and opto-electronic devices [4]. Iron pyrite (FeS_2) which is also known as Fool's gold is non-magnetic semiconductor. Its crystal structure resembles with the rock salt NaCl, where Na and Cl sites are occupied by Fe ion and S anion pairs, respectively. The electronic structure of FeS_2 has been investigated both theoretically and experimentally at room temperature and normal pressure [5–10]. Among later studies, Muscat et al. [11] have reported density-functional theory (DFT) calculations using plane wave pseudopotentials and Gaussian basis sets. Kokubun et al. [12] have measured the experimental anisotropy in the atomic scattering factor and compared their data with the *ab initio* calculations. Hung et al. [13] have computed the electronic properties using plane waves. Furthermore, X-ray absorption and emission spectroscopy based experimental studies on FeS_2 have been reported by several workers [14–18]. Although there have been few band structure calculations, the computation of momentum densities and hence the Compton profiles still remains untouched.

It is worth mentioning that Compton scattering is a well known probe to explain the ground state electron momentum distribution in metals, alloys and compounds [19]. Within the impulse approximation, the Compton profile is the projection of electron momentum density $\rho(\boldsymbol{p})$ and can be deduced from the spectral distribution of Compton scattered photons. The Compton profile technique has advantages like its insensitiveness to surface effects and crystal defects and also its applicability in low defect materials. The Compton profile, $J(p_z)$, is defined as

$$J(p_z) = \int_{p_x}\int_{p_y} \rho(\boldsymbol{p})\, dp_x dp_y, \tag{1}$$

where p_z is the component of the electron momentum along the scattering vector (chosen as the z-axis). In the absolute profiles, it may be difficult to identify the fine structures in the Compton line shapes. The anisotropy in the Compton profiles ($J_{hkl} - J_{h'k'l'}$) measured along crystallographic directions removes systematic problems like background contribution, failure of impulse approximation, residual effects of multiple scattering, etc.

* Corresponding author. Tel.: +91 294 2413955; fax: +91 294 2411950.
E-mail address: blahuja@yahoo.com (B.L. Ahuja).

0925-8388/$ – see front matter © 2010 Elsevier B.V. All rights reserved.
doi:10.1016/j.jallcom.2010.11.196

To explore the electronic properties of FeS_2 using electron momentum densities, in this paper, we report for the first time the experimental and theoretical directional Compton profiles of this pyrite. The anisotropy in the momentum densities is interpreted in terms of energy bands and density of states (DOS) computed using DFT approach at the level of linear combination of atomic orbitals (LCAO). To check the utility of FeS_2 in photovoltaics, we have also computed the optical properties (imaginary part of dielectric tensor and absorption coefficient) using full potential augmented plane wave (FP-LAPW) method.

2. Experiment

For the measurement of directional Compton profiles, the first-ever lowest intensity 100 mCi ^{241}Am Compton spectrometer [20] was used. Single crystals of FeS_2 ([1 1 0] and [1 0 0] directions) of thickness 4 mm and diameter 20 mm were received from Jim Porter of Warwick University, UK. The orientations of the samples were confirmed using X-ray diffraction. The incident photons of energy 59.54 keV were scattered from crystalline samples along Γ–M [1 1 0] and Γ–X [1 0 0] directions, at an angle $165 \pm 1.5^{\circ}$. The scattered photons were detected by a high purity Ge detector (HPGe, Canberra GL0210P). The diameter of incident beam at the sample position was kept to be about 8 mm. The overall momentum resolution of the spectrometer, which incorporates the detector resolution as well as the divergence of incident and scattered beams, was 0.55 a.u. (Gaussian full width at half maximum). To obtain the directional Compton profiles the single crystals along [1 0 0] and [1 1 0] directions were exposed by γ-rays for 119.4 and 141.0 h, respectively. The integrated Compton intensities for [1 0 0] and [1 1 0] directions were found to be 2.43×10^7 and 2.78×10^7 photons, respectively. To extract the true Compton profile, the raw data were corrected for background and a number of energy dependent corrections like instrumental resolution, sample absorption, scattering cross-section, etc. [19,21]. The instrumental resolution correction was limited to stripping off the low energy tail in the measured data. The effect of multiple (up to triple) scattering of photons in the sample was simulated by the Monte Carlo procedure [22] and subtracted from the profiles. The ratio of multiple to single scattering events (in the momentum range 0–10 a.u) was found to be 10.2%.

3. Computational methodology

3.1. LCAO calculations

The energy bands, DOS and Compton profiles of FeS_2 were calculated using LCAO method as embodied in CRYSTAL03 code [23]. This code makes use of local basis sets of Gaussian-type orbitals GTOs and is a reliable tool for computing the electronic and associated properties of variety of materials [see, for example, 23–25]. The code facilitates Hartree–Fock (HF) and DFT with a local density approximation (LDA) and a generalised gradient approximation (GGA). It may be noted that in HF scheme exact interaction between the electrons is accounted while the correlation effects are ignored.

In DFT approximation, the total ground state energy of an electron system is written as a functional of electron density $\rho(\boldsymbol{r})$. In case of DFT–LDA, the exchange–correlation density functional energy (E_{XC}) is defined from uniform $\rho(\boldsymbol{r})$ as

$$E_{XC}^{\mathrm{LDA}}[\rho(\boldsymbol{r})] = \int \rho(\boldsymbol{r})\varepsilon_{XC}[\rho(\boldsymbol{r})]d\boldsymbol{r} \quad (2)$$

In DFT–GGA approximation, the energy E_{XC} depends not only on $\rho(\boldsymbol{r})$ but also on gradient of $\rho(\boldsymbol{r})$.

Mathematically,

$$E_{XC}^{\mathrm{GGA}}[\rho(\boldsymbol{r})] = \int \rho(\boldsymbol{r})\varepsilon_{XC}[\rho(\boldsymbol{r}), |\nabla\rho(\boldsymbol{r})|]d\boldsymbol{r} \quad (3)$$

In the present DFT–LDA calculations, we have considered the exchange potential of Dirac–Slater [23] and the correlation potential of Perdew and Zunger [26], while in case of DFT–GGA both the exchange and correlation potentials were taken from Perdew et al. [27].

To see the role of hybrid HF/DFT method, we have also considered the B3LYP functional form, which involves Becke's three parameter hybrid exchange and Lee–Yang–Parr correlation functionals. Within the B3LYP scheme, the exchange–correlation energy E_{XC} is defined as [23]

$$E^{\mathrm{B3LYP}} = (1-a)\times(E_X^{\mathrm{LDA}} + b\times\Delta E_X^{\mathrm{BECKE}}) + a\times E_X^{\mathrm{HF}} + (1-c) \times E_C^{\mathrm{VWN}} + c\times E_C^{\mathrm{LYP}} \quad (4)$$

where $\Delta E_X^{\mathrm{BECKE}}$ is Becke's gradient correction to the exchange functional E_X^{LDA}. E_C^{LYP} and E_C^{VWN} are the correlation energies due to Lee–Yang–Parr [28] and Vosko–Wilk–Nusair [29], respectively. In Eq. (4), we have used the standard values of pre-factors ($a = 0.20$, $b = 0.90$ and $c = 0.81$). For faster convergence of self-consistence field (SCF) cycles, the BROYDEN scheme [30] was applied. The all electron Gaussian basis sets for Fe and S were taken from http://www.tcm.phy.cam.ac.uk/~mdt26/basis_sets/. The energy optimisation of the basis sets was undertaken using the BILLY software [23]. The optimised basis sets are given in Table 1. Following the default tolerances in the CRYSTAL03 code, the SCF calculations have been performed at 328k points in the irreducible Brillouin zone (IBZ). The lattice constant for FeS_2 (cubic structure with space group $Pa\bar{3}$) was taken as 5.416 Å [11].

The $\rho(\boldsymbol{r})$ was calculated from the sum of the squared moduli of the occupied crystalline orbitals in a momentum space represen-

Table 1
Optimised basis sets, Gaussian exponents (in a.u.$^{-2}$) and contraction coefficients for Fe and S in solid state FeS_2. Asterisks denote atomic orbitals assumed to be unoccupied at the beginning of the self consistent field process.

Atom	Orbitals	Exponents	Coefficients		
			s	p	d
Fe	1s	315379.0	0.000227		
		45690.0	0.0019		
		9677.3	0.0111		
		2520.88	0.0501		
		759.746	0.1705		
		262.964	0.36924		
		102.801	0.4033		
		42.9733	0.1434		
	2sp	798.262	−0.0052	0.00850	
		191.162	−0.068	0.0608	
		63.6885	−0.1314	0.2114	
		25.3625	0.2517	0.3944	
		10.7338	0.6433	0.398	
		3.764	0.2825	0.2251	
	3sp	48.1434	0.0122	−0.0215	
		17.4579	−0.2278	−0.085	
		6.9972	−0.8801	0.201	
		3. 0791	0. 9755	1.3024	
	4sp	1.2071	1.0	1.0	
	4sp*	0.3827	1.0	1.0	
	3d	33.8149			0.051
		9.2879			0.2566
		3.0936			0.5688
		1.036			0.6734
	3d*	0.2924			1.0
S	1s	109211.0	0.0002520		
		16235.206	0.0019934		
		3573.0286	0.0111177		
		943.23811	0.0498945		
		287.26179	0.1661455		
		99.914226	0.3627018		
		38.602137	0.4108787		
		15.531224	0.1457875		
	2sp	281.22171	−0.0057780	0.0081427	
		67.106575	−0.0665855	0.0565570	
		21.794135	−0.1203552	0.2039582	
		8.2097646	0.2741310	0.3973328	
		3.4178289	0.6463829	0.3946313	
		1.5452225	0.2925792	0.1544345	
	3sp	3.8509	−0.2047	−0.0955	
		1.4966	−0.4339	0.3543	
		0.564	1.0553	2.1747	
	3sp*	0.186	1.0	1.0	

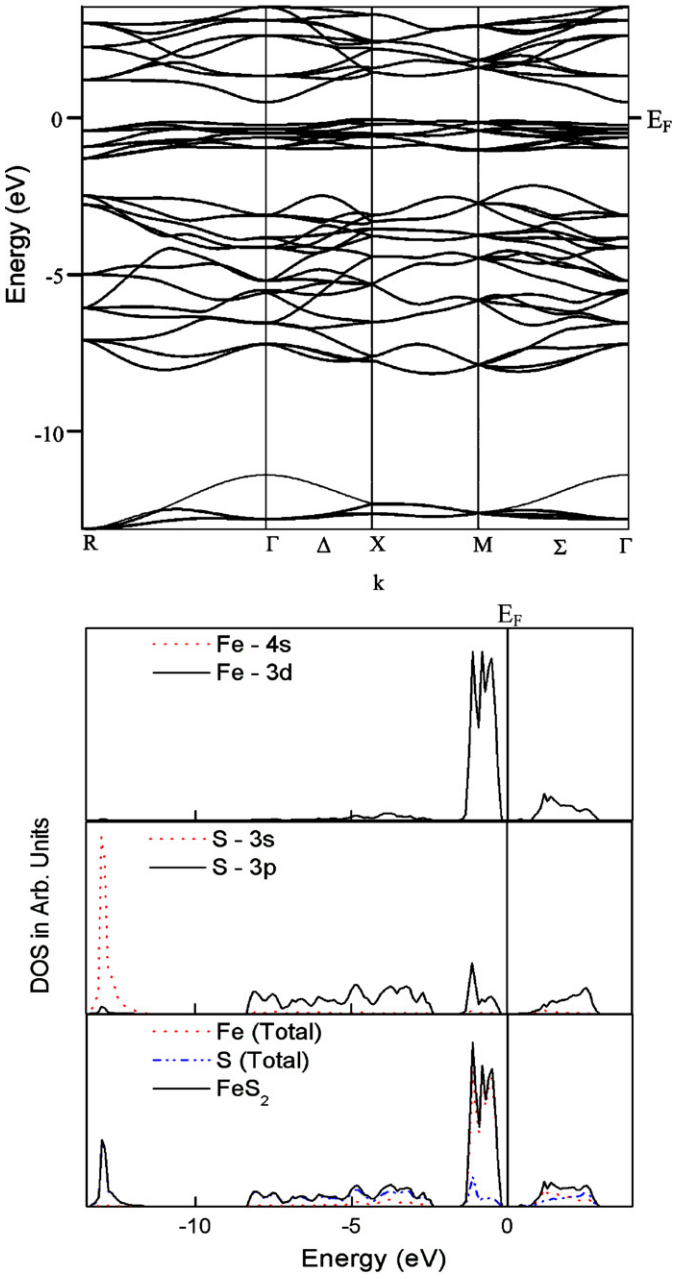

Fig. 1. Selected energy bands (E–k relation) along high symmetry directions of the first Brillouin zone using LCAO–DFT–GGA method for FeS_2. In the lower panel the total and partial density of states (DOS) are also shown. The positions of Γ, X, M and R vertices correspond to (0, 0, 0), (1/2, 0, 0), (1/2, 1/2, 0) and (1/2, 1/2, 1/2), respectively.

tation. Within the notations of CRYSTAL03 package [23], the $\rho(\boldsymbol{p})$ is expressed as

$$\rho(\boldsymbol{p}) = \frac{1}{\boldsymbol{V}_{\mathrm{BZ}}} \sum_j \int_{\mathrm{BZ}} d\boldsymbol{k} \left| \psi_j(\boldsymbol{k}, \boldsymbol{p}) \right|^2 \theta[\varepsilon_F - \varepsilon_j(\boldsymbol{k})] \quad (5)$$

where θ is the Heaviside step function, ε_F is the Fermi energy, $\varepsilon_j(\boldsymbol{k})$ is the $\boldsymbol{k}$-dependent eigen value of the jth orbital and $\boldsymbol{V}_{\mathrm{BZ}}$ stands for the volume of the BZ. An integration of $\rho(\boldsymbol{p})$, as given in Eq. (1), leads to Compton profiles. All the experimental and theoretical profiles were normalised to 26.39 e^- in the momentum range 0–7 a.u. [31].

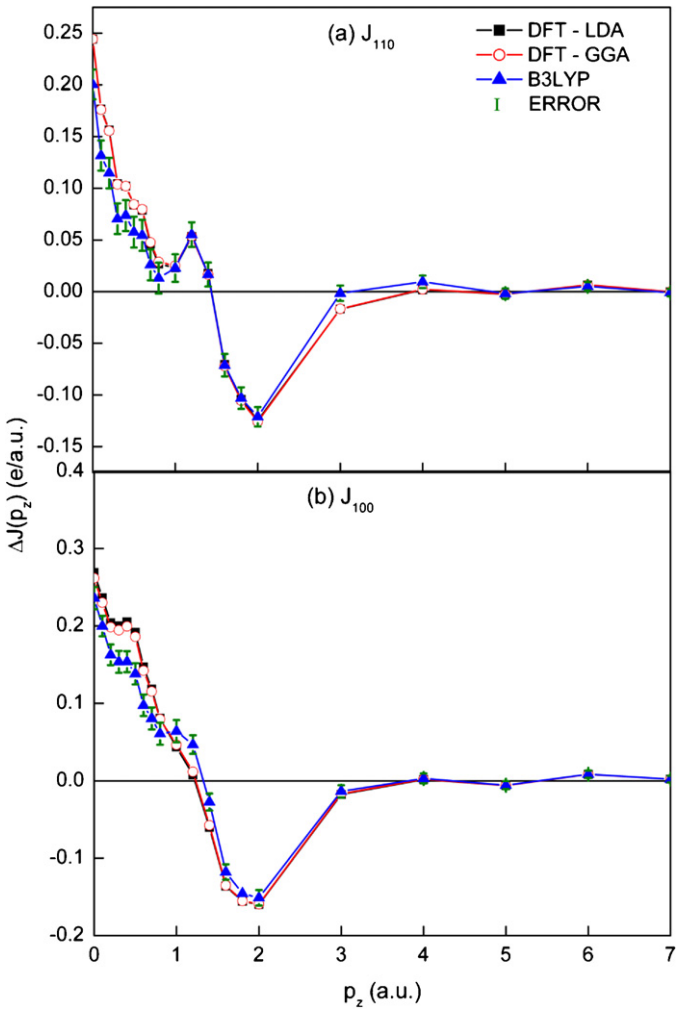

Fig. 2. Difference between the convoluted theoretical and experimental absolute Compton profiles for (a) J_{110} and (b) J_{100}. The statistical error ($\pm\sigma$) is also shown.

3.2. FP-LAPW calculations

In order to obtain the optical properties using FP-LAPW scheme, we have used the WIEN2k code [32]. In this formalism, we have also used local orbitals (*lo*) for the high lying semi-core states. This method is supposed to give accurate results for optical properties because no shape approximation is made for the potential or charge density. The radius of Muffin-tin sphere (R_{MT}) was chosen to be 2.26 a.u. for Fe and 2.00 a.u. for S. Like LCAO, we have used GGA functional in FP-LAPW as proposed by Perdew et al. [27]. It may be noted that these functionals have no adjustable parameters and are based on a diffuse radial cut off for the exchange hole in real space. Moreover, an analytic expansion of the exchange energy for small gradients is accounted in these functionals. The convergence criterion was set to 0.01 m*Ry* which is sufficient due to use of *lo* and APWs. In the present calculations, 249 ($7 \times 7 \times 7$) $\boldsymbol{k}$ points were considered in the irreducible wedge of BZ. The value of $R_{\mathrm{MT}}K_{\mathrm{max}}$ was kept equal to 7 (K_{max} is the maximum modulus of reciprocal lattice vector). The maximum radial expansion was set equal to 10.

To derive the optical properties, one needs to calculate mainly the frequency dependent dielectric function $\varepsilon(\omega)$ [33] which is given as

$$\varepsilon(\omega) = \varepsilon_1(\omega) + i\varepsilon_2(\omega) \quad (6)$$

The imaginary or absorptive part of frequency-dependent dielectric function $\varepsilon_2(\omega)$ depends on the joint density of states and

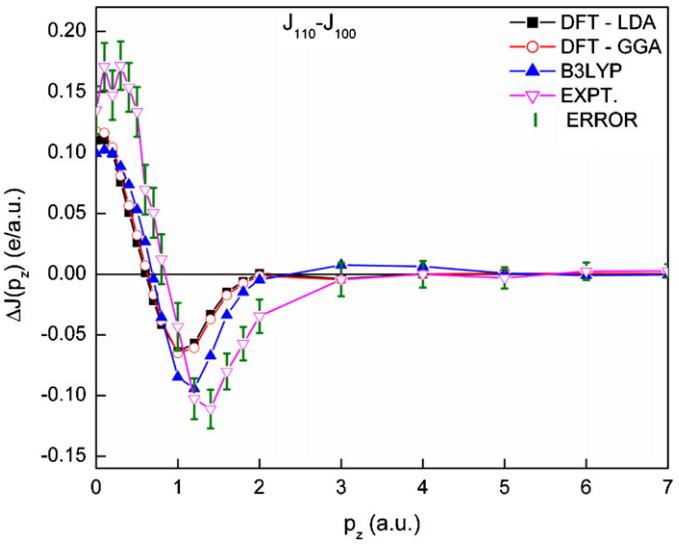

Fig. 3. Experimental and theoretical Compton profile anisotropies ($J_{110} - J_{100}$) for FeS_2. Before deducing the anisotropies, the theoretical profiles have been convoluted with a Gaussian function of FWHM 0.55 a.u. The statistical error in the experimental data ($\pm\sigma$) is also shown.

the momentum matrix elements. The direct interband contribution to the $\varepsilon_2(\omega)$ is calculated by summing up all possible transitions from occupied to unoccupied states,

$$\varepsilon_2(\omega) = \frac{e^2\hbar}{\pi m^2\omega^2}\sum_{v,c}\int_{BZ}\left|M_{cv}(k)\right|^2\delta[\omega_{cv}(k)-\omega]d^3k. \quad (7)$$

The integral is taken over the first BZ. The momentum dipole elements are represented by $M_{cv}(k)$. The transition energy $\hbar\omega_{cv}(k)$ is derived from the valence and conduction bands. The real component $\varepsilon_1(\omega)$ is obtained using the Kramers–Kronig relations which is defined as,

$$\varepsilon_1(\omega) = 1 + \frac{2}{\pi}P\int_0^\infty \frac{\omega'\varepsilon_2(\omega')}{\omega'^2-\omega^2}d\omega'. \quad (8)$$

Here P denotes the principal value of the integral.

The absorption coefficient which plays a major role in optical properties is given by

$$I(\omega) = 2\omega\left(\frac{[\varepsilon_1(\omega)+\varepsilon_2(\omega)]^{1/2}-\varepsilon_1(\omega)}{2}\right)^{1/2}. \quad (9)$$

It is worth mentioning that Wien2k code does not facilitate the computation of momentum densities.

4. Results and discussion

4.1. Energy bands and Compton profiles

In Fig. 1, we have presented energy bands and DOS of FeS_2 using LCAO–DFT–GGA. The topology of energy bands from other LCAO based calculations is almost same; therefore we have not shown them. Cross-over of energy bands along the two special symmetry directions [1 1 0] (Γ–M in the first BZ) and [1 0 0] (Γ–X) make the energy bands quite interesting. In Fig. 1, the energy bands are found in different groups with several degenerate states. From the DOS curves, it can be seen that the lowest bands originate mainly from anion S 3s states, while the second group of bands mainly consists of S 3p states. The top most group of valence bands is formed by Fe 3d and S 3p states, with major contribution from the Fe 3d. The region close to Fermi level is dominated by fully occupied Fe $3d_{z^2}$ states (separately not shown) with a small admixture of S 3p states. The conduction bands mainly arise from the hybridised Fe $3d_{x^2y^2} + d_{xy}$, $3d_{xz+yz}$ and S 3p antibonding states. Fig. 1 also depicts that electronic properties of FeS_2 are dominated strongly by hybridisation of Fe 3d and S 3p states. Now we compare our experimental and theoretical Compton profiles and interpret them in terms of energy bands.

The theoretical directional Compton profiles computed within the frame work of DFT with LDA, GGA and hybrid HF/DFT (B3LYP) method using CRYSTAL03 code are listed in Table 2. For an extensive use of our experimental data, we have also incorporated the numerical values of our experimental Compton profiles. In this table, the experimental values of J_{110} and J_{100} at $p_z = 0$ are found to be 13.638 ± 0.014 e/a.u. and 13.463 ± 0.014 e/a.u., respectively. This data can be understood by the fact that the projection of the momentum density along [1 1 0] so-called $J_{110}(p_z)$ is greater than $J_{100}(p_z)$, which shows that electrons are more delocalised in position space in [1 1 0] direction. In Fig. 2, we have plotted the difference between the convoluted theory and the experiment for (a) [1 1 0] and (b) [1 0 0] directions. From Fig. 2, it is clearly seen

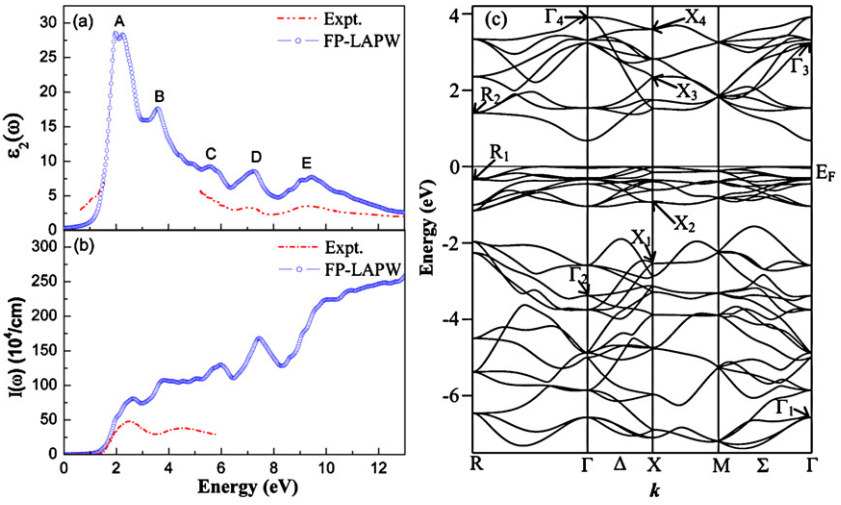

Fig. 4. (a) Dielectric function $\varepsilon_2(\omega)$, (b) absorption coefficient $I(\omega)$ and (c) energy bands of FeS_2 computed using FP-LAPW method.

Table 2
Experimental and theoretical (unconvoluted) directional Compton profiles of FeS_2. For comparison with the present experiment, all the theoretical profiles are convoluted with a Gaussian FWHM of 0.55 a.u.

p_z (a.u.)	$J(p_z)$ (in e/a.u.)							
	[100]				[110]			
	DFT–LDA	DFT–GGA	B3LYP	Expt.	DFT–LDA	DFT–GGA	B3LYP	Expt.
0.0	13.877	13.870	13.844	13.463 ± 0.014	13.877	13.988	13.944	13.638 ± 0.014
0.1	13.735	13.729	13.698	13.517 ± 0.014	13.735	13.845	13.801	13.653 ± 0.014
0.2	13.522	13.517	13.481	13.339 ± 0.014	13.522	13.621	13.580	13.531 ± 0.014
0.3	13.234	13.228	13.188	12.964 ± 0.014	13.234	13.309	13.276	13.192 ± 0.014
0.4	12.855	12.849	12.804	12.564 ± 0.014	12.855	12.906	12.877	12.728 ± 0.014
0.5	12.373	12.367	12.319	12.166 ± 0.014	12.373	12.399	12.372	12.241 ± 0.014
0.6	11.786	11.782	11.737	11.641 ± 0.014	11.786	11.789	11.764	11.696 ± 0.014
0.7	11.110	11.106	11.072	10.936 ± 0.014	11.110	11.089	11.068	11.033 ± 0.014
0.8	10.365	10.364	10.346	10.180 ± 0.014	10.365	10.326	10.310	10.273 ± 0.014
1.0	8.802	8.805	8.822	8.748 ± 0.014	8.802	8.740	8.738	8.691 ± 0.013
1.2	7.350	7.354	7.389	7.154 ± 0.012	7.350	7.293	7.295	7.228 ± 0.012
1.4	6.175	6.178	6.208	6.226 ± 0.011	6.175	6.141	6.141	6.146 ± 0.012
1.6	5.304	5.305	5.322	5.289 ± 0.010	5.304	5.288	5.289	5.353 ± 0.011
1.8	4.669	4.669	4.679	4.781 ± 0.010	4.669	4.662	4.664	4.779 ± 0.010
2.0	4.177	4.178	4.186	4.325 ± 0.010	4.177	4.176	4.181	4.300 ± 0.009
3.0	2.589	2.590	2.593	2.620 ± 0.008	2.589	2.585	2.601	2.612 ± 0.007
4.0	1.658	1.658	1.659	1.722 ± 0.006	1.658	1.658	1.666	1.661 ± 0.006
5.0	1.128	1.128	1.129	1.170 ± 0.005	1.128	1.129	1.129	1.153 ± 0.005
6.0	0.806	0.806	0.806	0.797 ± 0.005	0.806	0.806	0.805	0.800 ± 0.004
7.0	0.611	0.611	0.611	0.594 ± 0.004	0.611	0.611	0.610	0.562 ± 0.004

that the calculations based on various schemes of DFT, namely LDA, GGA and B3LYP give almost similar trend. All the theoretical profiles overestimate the momentum densities in the vicinity of $p_z = 0$ a.u., while a reverse trend is seen in the intermediate momentum range 1.4–3.0 a.u. This means that there may be few electrons partially occupying the region just above the Fermi level. This can be partly explained by thermal excitations, which are not accounted in our theoretical calculations. Further, the LCAO calculations are non-relativistic and in Kohn–Sham DFT approximation there is approximate inclusion of exchange and correlation effects. To check the best agreement between theory (J^{Th}) and experiment (J^{Expt} with $\pm\sigma$ error), we have also made χ^2 fitting which is defined as

$$\chi^2 = \sum_{p_z=0}^{7} \left[\frac{J^{Th}(p_z) - J^{Expt}(p_z)}{\sigma(p_z)} \right]^2 . \quad (10)$$

The summation extends over the experimental data points.

On the basis of χ^2 fitting, it is seen that B3LYP gives the best agreement (overall) with the experiment. The experimental anisotropies ($J_{110} - J_{100}$) along with theoretical data are plotted in Fig. 3. In the low momentum region, the experimental data show higher magnitude of anisotropy in comparison to DFT calculations. The overall trend of the experimental anisotropy is again well approximated by the B3LYP. Within the limitations of the instrumental resolution, the periodicity in anisotropies $J_{110} - J_{100}$ (Fig. 3) can be understood mainly in terms of energy bands, their crossings and degenerate states in ΓX [1 0 0] and ΓM [1 1 0] branches. Due to large number of allowed states and cross-overs of bands in ΓM branch in comparison to ΓX (Fig. 1), there is higher value of electron density which enhances the electron momentum density (and hence the Compton profile) in the low momentum region of [1 1 0] direction. It leads to positive amplitude of the anisotropy $J_{110} - J_{100}$ near $p_z = 0$ as evident from Fig. 3. Using similar logic, the negative oscillation in $J_{110} - J_{100}$ at about 1.2 a.u. is attributed to degenerate states in ΓX (=0.307 × n a.u. where $n = 4$) branch.

4.2. Optical properties

In Fig. 4(a) and (b), we present frequency dependent dielectric function and absorption coefficient calculated using the FP-LAPW method. First of all, we discuss the imaginary part of the dielectric function $\varepsilon_2(\omega)$ of FeS_2 as shown in Fig. 4(a). In this curve, five intense peaks are marked as A (at 2 eV), B (at 3.6 eV), C (at 5.5 eV), D (at 7.2 eV) and E (about 9.4 eV). The formation of these peaks can be explained on the basis of interband transitions in energy bands computed using FP-LAPW scheme (Fig. 4c). Peak A may be due to the transitions from $R_1 \rightarrow R_2$ (Fe 3d → S 3p). The transition $X_2 \rightarrow X_3$ (Fe 3d → S 3p) originates the peak B. The peak C arises due to transition from $X_1 \rightarrow X_4$. The origin of peak D may be understood in terms of transition from $\Gamma_2 \rightarrow \Gamma_4$. Transition from S 3p states to Fe 3d states ($\Gamma_2 \rightarrow \Gamma_3$) gives the broad peak E. It is seen that all the transitions are mainly between S 3p and Fe 3d states. All these transitions follow the dipolar selection rule which states that only transitions changing the angular momentum quantum number l by unity ($\Delta l = \pm 1$) are allowed. Our theoretical calculations show a reasonable agreement with the ultraviolet reflectance spectra measured by Suga et al. [34] at SOR-RING synchrotron radiation facility. Now we explain the absorption coefficient $I(\omega)$ (Fig. 4b) along with the spectrophotometer based absorption measurements reported by Ferrer et al. [35]. A comparison of FP-LAPW and experimental absorption coefficients shows that the theoretical absorption starts at about 0.60 eV while the corresponding experimental value is found to be 0.70 eV. It is also observed that the amplitude of experimental absorption data is lower than that computed using FP-LAPW method. Such type of discrepancy can occur due to the broadening of the experimental data which may influence the intensity of peaks. It is worth noting that, larger smearing width significantly lowers the intensity of such peaks. In the low energy region (<3 eV), the overall features in the experimental data are similar to FP-LAPW computations. It is known that most of the intense part of the sun's emission emerges in the energy range 0–5 eV. A reasonable value of theoretical absorption coefficient between 3 and 4 eV confirms the suitability of FeS_2 in fabrication of solar cells. Therefore, the present optical data support the predictions related to utility of FeS_2 in solar cells as reported by Ennaoui et al. [36].

5. Conclusions

We have computed the directional momentum densities of FeS_2 using density functional theory. Our measurement on directional Compton profiles shows a good agreement with the hybrid

Hartree–Fock and density functional theory. The anisotropy in the Compton profiles is partly explained in terms of energy bands. Like absolute profiles, experimental anisotropy in Compton profiles also shows a better agreement with the hybrid functionals. The optical properties computed using FP-LAPW method with the GGA functionals of Perdew et al. are in agreement with the available experimental data. Reasonable value of absorption coefficients of FeS_2 in the energy range 3–4 eV shows its usefulness in the fabrication of solar cells. Synchrotron based high resolution Compton profile measurements and relativistic band structure calculations may further be helpful.

Acknowledgements

One of us (LV) is grateful to CSIR, New Delhi for Senoir Research Fellowship. This work is supported by CSIR, New Delhi vide grant no. 03(1157)/10/EMR-II. We are also grateful to Prof. R. Dovesi and Prof P. Blaha, and the respective Support Teams for providing the CRYSTAL03 and WIEN2k codes. Help provided by Dr. N.L. Heda, Dr. M. Sharma, Mr. V. Sharma, Ms. Alpa Dashora and Dr. Yamini Sharma is also acknowledged.

References

[1] V. Eyert, K.-H. Hock, S. Fiechter, H. Tributsch, Phys. Rev. B 57 (1998) 6350–6359.
[2] J.A. Wilson, A.D. Yoffe, Adv. Phys. 18 (1969) 193–335.
[3] S.K. Srivastava, B.N. Avasthi, J. Mater. Sci. 23 (1985) 3801–3815.
[4] H. Tributsch, Z. Naturforsch. A 32 (1977) 972–985.
[5] G. Will, J. Lauterjung, H. Schmitz, E. Hinze, in: C. Homan, R.K. MacCrone, E. Whalley (Eds.), Materials Research Society Symp. Proc., vol. 22, Elsevier, New York, 1984.
[6] G.L. Zhao, J. Callaway, M. Hayashibara, Phys. Rev. B 48 (1993) 15781–15786.
[7] M. Womes, R.C. Karnatak, J.M. Esteva, I. Lefebvre, G. Allan, J. Olivier-Fourcades, J.C. Jumas, J. Phys. Chem. Solids 58 (1997) 345–352.
[8] A. Schlegel, P. Wachter, J.Phys. C.: Solid State Phys. 9 (1976) 3363–3369.
[9] I. Opahle, K. Koepernik, H. Eschrig, Phys. Rev. B 60 (1999) 14035–14041.
[10] P. Cervantes, Z. Slanic, F. Bridges, E. Knittle, Q. Williams, J. Phys. Chem. Solids 63 (2002) 1927–1933.
[11] J. Muscat, A. Hung, S. Russo, I. Yarovsky, Phys. Rev. B 65 (2002) 054107–054118.
[12] J. Kokubun, K. Ishida, D. Cabaret, F. Mauri, R.V. Vedrinskii, V.L. Kraizman, A.A. Novakovich, E.V. Krivitskii, V.E. Dmitrienko, Phys. Rev. B 69 (2004) 245103–245116.
[13] A. Hung, J. Muscat, I. Yarovsky, S.P. Russo, Surf. Sci. 513 (2002) 511–524.
[14] E.Z. Kurmaev, J. van Ek, D.L. Ederer, L. Zhou, T.A. Callcott, R.C.C. Perera, V.M. Cherkashenko, S.N. Shamin, V.A. Trofimova, S. Bartkowski, M. Neumann, A. Fujimori, V.P. Moloshag, J. Phys.: Condens. Matter 10 (1998) 1687–1697.
[15] S. Suga, A. Kimura, T. Matsushita, A. Sekiyama, S. Imada, K. Mamiya, A. Fujimori, H. Takahashi, N. Mori, Phys. Rev. B 60 (1999) 5049–5054.
[16] K.C. Prince, K. Kuepper, M. Neumann, D. Cocco, F. Bondino, M. Zangrando, M. Zacchigna, M. Matteucci, F. Parmigiani, J. Phys.: Condens. Matter 16 (2004) 7397–7404.
[17] K.C. Prince, M. Matteucci, K. Kuepper, S.G. Chiuzbaian, S. Bartkowski, M. Neumann, Phys. Rev. B 71 (2005) 085102–085110.
[18] G.U. von Oertzen, W.M. Skinner, H.W. Nesbitt, Phys. Rev. B 72 (2005) 235427–235437.
[19] M.J. Cooper, P.E. Mijnarends, N. Shiotani, N. Sakai, A. Bansil, X-ray Compton Scattering, Oxford University Press, New York, 2004.
[20] B.L. Ahuja, V. Sharma, A. Rathor, A.R. Jani, B.K. Sharma, Nucl. Instrum. Methods B 262 (2007) 391–398.
[21] B.G. Williams (Ed.), Compton Scattering, McGraw-Hill, London, 1977.
[22] J. Felsteiner, P. Pattison, M.J. Copper, Phil. Mag. 30 (1974) 537–548.
[23] V.R. Saunders, R. Dovesi, C. Roetti, R. Orlando, C.M. Zicovich-Wilson, N.M. Harrison, K. Doll, B. Civalleri, I. Bush, Ph. D'Arco, M. Llunell, CRYSTAL03 User's Manual, University of Torino, Torino, 2003, and references therein;
M.D. Towler, A. Zupan, M. Causa, Comp. Phys. Commun. 98 (1996) 181–205.
[24] M. Harb, P. Labeguerie, I. Baraille, M. Rerat, Phys. Rev. B 80 (2009) 235131–235137.
[25] T. Shimazaki, Y. Asai, J. Chem. Phys. 132 (2010) 224105–224111.
[26] J.P. Perdew, A. Zunger, Phys. Rev. B 23 (1981) 5048–5079.
[27] J.P. Perdew, K. Burke, M. Ernzerhof, Phys. Rev. Lett. 77 (1996) 3865–3868.
[28] C. Lee, W. Yang, R.G. Parr, Phys. Rev. B 37 (1988) 785–789.
[29] S.H. Vosko, L. Wilk, M. Nusair, Can. J. Phys. 58 (1980) 1200–1211.
[30] D.D. Johnson, Phys. Rev. B 38 (1988) 12807–12813.
[31] F. Biggs, L.B. Mandelsohn, J.B. Mann, Atom. Data Nucl. Data Tables 16 (1975) 201–308.
[32] P. Blaha, K. Schwarz, J. Luitz, WIEN code, An Augmented Plane Wave Plus Local Orbitals Program for Calculating Crystal Properties, Vienna University of Technology, Vienna, Austria, 2001;
P. Blaha, K. Schwarz, P. Sorantin, S.B. Trickey, Comput. Phys. Commun. 59 (1990) 399–415.
[33] C. Amrosch-Draxl, J.O. Sofo, Comput. Phys. Commun. 175 (2006) 1–14.
[34] S. Suga, K. Inoue, M. Taniguchi, S. Shin, M. Seki, K. Sato, T. Teranishi, J. Phys. Soc. Jpn. 52 (1983) 1848–1856.
[35] I.J. Ferrer, D.M. Nevskaia, C. de las Heras, C. Sanchez, Solid State Commun. 74 (1990) 913–916.
[36] A. Ennaoui, S. Fiechter, Ch. Pettenkofer, N. Alonso-Vante, K. Bilker, M. Bronold, Ch. Höpfner, H. Tributsch, Sol. Energy Mater. Sol. Cells 29 (1993) 289–370.